

# Micromagnetic Measurements of ferromagnetic materials: validation of a 3D numerical model

Massimiliano d'Aquino<sup>1</sup>, Simone Minucci<sup>2</sup>, Carlo Petrarca<sup>3,\*</sup>, Guglielmo Rubinacci<sup>3</sup>, Antonello Tamburrino<sup>4,5</sup>, and Salvatore Ventre<sup>4,+</sup>

<sup>1</sup>DING, Università degli Studi di Napoli "Parthenope", Napoli, ITALY

<sup>2</sup>DEIM, Università degli Studi di Viterbo TUSCIA, Viterbo, ITALY

<sup>3</sup>DIETI, Università degli Studi di Napoli FEDERICO II, Napoli, ITALY

<sup>4</sup>DIEI, Università degli Studi di Cassino e del Lazio Meridionale, Cassino, ITALY

<sup>5</sup>ECE, Michigan State University, East Lansing, Michigan, USA

Corresponding authors:

\* [carlo.petrarca@unina.it](mailto:carlo.petrarca@unina.it)

+ [salvatore.ventre@unicas.it](mailto:salvatore.ventre@unicas.it)

**Abstract**– This work is focused on (nondestructive) micromagnetic measurements for ferromagnetic materials in view of Material Characterization (MC). The interest in micromagnetic measurements arises from their correlation to mechanical properties. It is well known that the microstructure of a material affects both the mechanical and magnetic properties, therefore it is possible to infer the mechanical properties from micromagnetic measurements. This is very convenient because micromagnetic measurements can be carried out in a fast, cheap and nondestructive manner, if compared to mechanical measurements. To date, a lot of experimental work has been carried in the past years but there is still some lack of proper numerical models capable of modelling micromagnetic measurements, especially when considering 3D models. In this paper we present an experimental validation of an ad-hoc 3D numerical model capable of modelling the response in micromagnetic characterization of ferromagnetic materials.

## 1. Introduction

Micromagnetic measurements (MM) are playing an important role in Material Characterization thanks to their capability of predicting mechanical properties such as hardness, yield strength or residual stress in a fast, cheap and nondestructive manner [1]. This makes MM very attractive in areas such as steel industry or nuclear industry, where obtaining information about the mechanical properties of materials without using expensive (mechanical) destructive test is a major goal for safety, quality control, optimization of production settings, etc. So far, MM have been applied to characterize aging phenomena such as creep degradation, thermal aging, degradation from neutron irradiation, fatigue degradation, case hardening depth estimation, etc.

MM have been extensively studied mainly from the experimental perspective, several devices and observable have been proposed [2, 3, 4, 5]. Common properties correlated to mechanical properties are measured from harmonic analysis, incremental permeability along the hysteresis loop, multi-frequency eddy current analysis and Barkhausen noise [1, 2, 6-11].

Numerical models capable to catch the underlying mechanisms are still a subject of active research. They are attractive because allow to lay the foundation for a better understanding of the link between magnetic properties and measured quantities. In addition to be a tool for a reliable interpretation of the measurements, they represent a tool to analyze current devices or to optimize new probe and systems.

Nowadays several 2D numerical models are available, although they are not capable of modeling the vectorial nature of the hysteresis ([12, 13]). Moreover, only few full 3D numerical models are available. This is because their development is a challenging problem for several reasons such as their high computational cost, the inherent complexity in modelling the constitutive magnetic relationship (nonlinear, hysteretic and vectorial), the presence of a strong skin-effect, etc.

Among the latest developments in this field (3D numerical modelling for MC through MM), we mention [14], a 3D code where the authors approximated the ferromagnetic material by a scalar and non-hysteretic model, and [20, 21, 22]. These latter contributions, which are the base for the numerical model treated in this work, rely on an (nonlinear and hysteretic) integral formulation of the problem. Specifically, the unknowns of the formulation are the induced eddy current density and the magnetization. The hysteresis is modeled through the vector extension of the Jiles-Atherton model and the code is optimized for period regimes.

We also mention [15] and [16] where the authors proposed a dynamic magnetic scalar hysteresis based on an extension of the Jiles-Atherton or Preisach models, respectively. Other recent developments about magnetic hysteresis models can be found in [17] and [18].

The contribution is organized as follows: in Section 2 the experimental setup is described with plenty of details together with a set of experimental results. In Section 3 the numerical model is briefly summarized and in Section 4 a comparison between numerical and experimental results is provided. The comparison proves the effectiveness of the numerical model thus, “promoting” it as computational tool for a better understanding of the physics of the (complex) probe-specimen interaction.

## **2. The Experimental Setup**

The experimental test-bed has been built in the “Laboratory of Circuits” at the University of Naples Federico II. In the following we provide a detailed description of its main components and circuits, together with the characterization of the materials and probes involved. Finally, a set of experimental results is illustrated and commented.

### *2.1. Main components and circuits*

A sketch of a typical probe used for testing ferromagnetic materials, together with the setup prepared in the laboratory, is shown in Fig. 1. It consists of a C-shaped ferromagnetic yoke placed above a conducting ferromagnetic specimen. An excitation (magnetization) coil is fed by a suitable Low Frequency (LF) time periodic voltage source which creates a strong magnetic field. It establishes a working point on the hysteresis cycle of the ferromagnetic specimen. A small pick-up and excitation coil is placed between the legs of the yoke

and is fed by a High Frequency (HF) sinusoidal current. An estimation of the incremental permeability  $\mu_{\Delta}$  at each point of the main hysteresis loop can be obtained by measuring the impedance of the HF coil. .

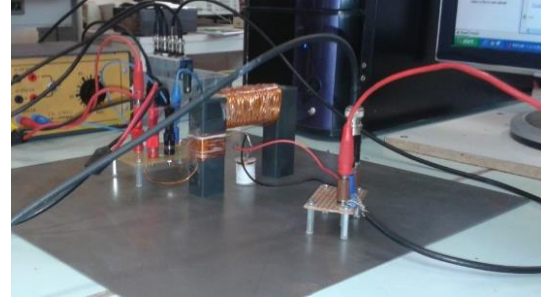
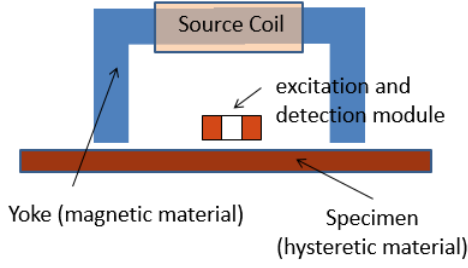


Fig.1. Left: sketch of a typical probe. Right: the experimental test bed.

The main components of the setup are represented in the block diagram of Fig. 2. The LF circuits feeds the excitation winding set on the C-shaped ferromagnetic yoke; the HF circuit excites a coil placed between the legs of the yoke; the probe stands on the Device Under Test (DUT). The test object, as will be clear in the following, can be either a ferromagnetic plate or a strip. Moreover, additional detection windings can be placed on the probe. All data are acquired by a DAQ module.

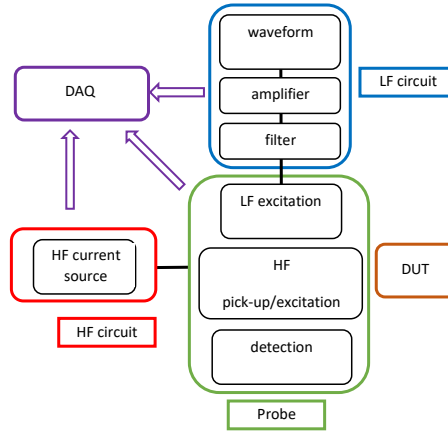


Fig. 2. Block diagram of the experimental setup.

In the following a detailed description of each part of the setup is given.

### 2.1.1. Low Frequency circuit

The LF circuit feeds the primary excitation coil placed on the ferromagnetic yoke with the LF voltage  $v_{lf}(t)$ . The low frequency excitation must be sufficient to reach saturation ( $B \sim 1.6 T$ ) in the test sample. The schematic of the circuit is represented in Fig. 3. The voltage generation stadium consists of a waveform generator (Tektronix AFG3022), which provides a sinusoidal voltage  $E_{lf}(t)$  with tunable amplitude and tunable frequency, and an electronic high-power amplifier (Kepco BOP 100-4M, 400 W), which increases the electric power related to the voltage source.

A band-pass filter is cascaded between the amplifier and the LF excitation winding (pictured as the inductor  $L$  in Fig. 3). The  $C1$  capacitor cuts the DC component of the source voltage, coming from any electronic

disturbance inside the waveform generator and the electronic amplifier as well. The C2 capacitor aims to create a recirculation for the HF current component coming from the magnetic coupling acting inside the probe.

A resistor R is connected in series with the LF excitation winding; it is used as a shunt to measure the LF excitation current. Its value must be a trade-off between the resolution of the data acquisition board and the need to reduce the harmonic content in the LF excitation voltage.

### 2.1.2. High Frequency circuit

The HF circuit feeds, with a HF voltage  $v_{hf}(t)$ , the HF pick-up excitation/detection coil placed between the legs of the ferromagnetic yoke. The generation stadium consists of a voltage driven current source, built by means of an operational amplifier TL082, since in this case a low power output is required (Fig. 3). The voltage  $E_{hf}(t)$  is the output of a waveform generator (Tektronix AFG3022). The resistor R3 is used as a shunt resistor to measure the HF excitation current. Also, the circuit can also be used as LF current generator. In such a case the input from the waveform generator must be a LF voltage, while the output current is used as input to the high power amplifier (Kepco BOP 100-4M).

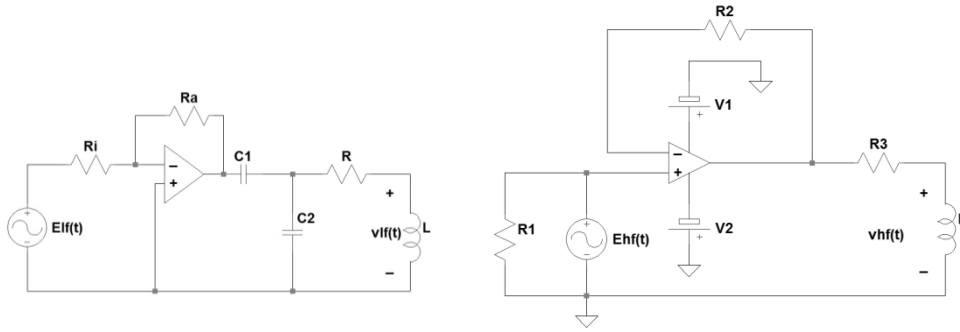


Fig. 3. Left: Schematic of the LF circuit ( $C1=10\text{mF}$ ,  $C1=10\text{mF}$ ,  $R=75\text{ m}\Omega$ ;  $R_i=2200\text{ }\Omega$ ;  $R_a=2200\text{ }\Omega$ ). Right: Schematic of the HF circuit ( $R1=200\text{ }\Omega$ ,  $R2=1500\text{ }\Omega$ ,  $R3=470\text{ }\Omega$ ).

### 2.1.3. Magnetic Probe

The yoke is made out of a soft magnetic material (NiZn) of cross section  $S = 28\text{mm} \times 20\text{mm}$ . The dimensions of the yoke are summarized in Fig. 4. The probe can be placed either on a ferromagnetic strip or on a ferromagnetic plate (Fig. 4). It is energized at Low Frequency with a coil of  $N_1$  turns. In order to detect the magnetic flux across the yoke, a pick-up coil  $N_2$  is wound across one leg. The HF excitation/detection coil is realized with  $N_3$  turns and is placed between the legs of the yoke. If possible, different detection and/or excitation coils ( $N_4$ ) can be used for a better understanding of the physical system under test.

### 2.1.4. Data Acquisition Board

The data acquisition board allows the recording of the time evolution of each variable of interest (supply voltages, induced voltages, excitation currents). A modular National Instruments USB system (NI CompactDAQ with 2 NI9222 input modules, 500 kHz, 16 bits) has been used: each input channel has its own Analog to Digital converter enabling the simultaneous recording of the following 8 variables:  $E_{lf}(t)$  (LF supply

voltage),  $i_{lf}(t)$  (LF excitation current),  $v_{lf}(t)$  (LF voltage at excitation winding  $N_1$ ),  $v_2(t)$  (induced voltage on pick-up winding  $N_2$ ),  $E_{hf}(t)$  (HF supply voltage),  $i_{hf}(t)$  (HF excitation current),  $v_{hf}(t)$  (HF voltage at excitation coil  $N_3$ ),  $v_4(t)$  (induced voltage on pick-up winding  $N_4$ ). A specific software developed within the MATLAB® environment manages the experiment control and the data acquisition.

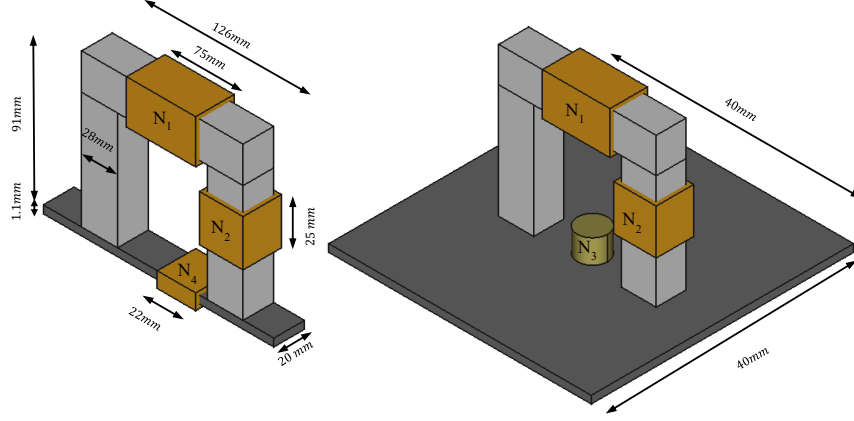


Fig. 4. Geometry of ferromagnetic yoke and test samples. Left: strip. Right: plate. The number of windings is:  $N_1=189$ ,  $N_2=38$ ,  $N_3=750$  and  $N_4=30$ .

## 2.2. Preliminary characterization

A detailed and accurate characterization of each component and each material involved in the setup has been carried out before any measurement. It is a mandatory task to correctly develop the numerical model.

### 2.2.1. Ferromagnetic sample

An Epstein frame has been used for the magnetic characterization of the material under test: 4 strips ( $250\text{mm} \times 20\text{mm} \times 1.1\text{mm}$ ) have been cut from the sample and overlapped in a BROCKHAUS Epstein frame. The hysteresis cycles, describing minor and major loops, obtained at 10 Hz for different values of the applied magnetic field, are presented in Fig. 5. In particular, all measurements have been performed by providing a sinusoidal voltage at the output of a Tektronix AFG3022, with rms value ranging between 100 mV and 2100 mV in steps of 200 mV. From the outer cycle we find that the mean saturation field is about  $B_S = 1.6\text{ T}$  while the coercive field is  $H_C = 300\text{ A/m}$ . As shown in the following section, such data have been used to derive the parameters of the Jiles-Atherton model adopted in the numerical model.

The electrical resistivity of the sample has been measured with a voltmeter-ammeter method by adopting a 4-probe system. Different measurements have been carried out at room temperature and at various values of the supply current. The resulting electrical resistivity is  $\eta_{Fe} = 12.4 \cdot 10^{-8}\ \Omega\text{m}$ .

### 2.2.2. Ferromagnetic yoke

The magnetic characterization of the C-shaped yoke has been performed by closing the magnetic circuit with the addition of an I-shaped bar having the same cross section and made out of the same ferromagnetic material. The time evolution of the LF magnetic field  $H(t)$  has been obtained by applying the Ampère law along the average magnetic path of length  $L_a = 374\text{ mm}$  and by measuring the excitation current  $i_{lf}(t)$ . Conversely, the

time evolution of the magnetic flux density field  $B(t)$  has been obtained by applying the Faraday-Neumann-Lenz to the induced voltage  $v_2(t)$  across the terminals of the pick-up winding  $N_2$ .

The resulting hysteresis loop plotted in Fig. 5 clearly shows that losses in the yoke can be neglected if compared to losses in the test samples and that the yoke can be approximated by a piece-wise linear characteristic. The mean saturation field is about  $B_S = 0.45 \text{ T}$ , while the coercive field is  $H_C = 15 \text{ A/m}$ .

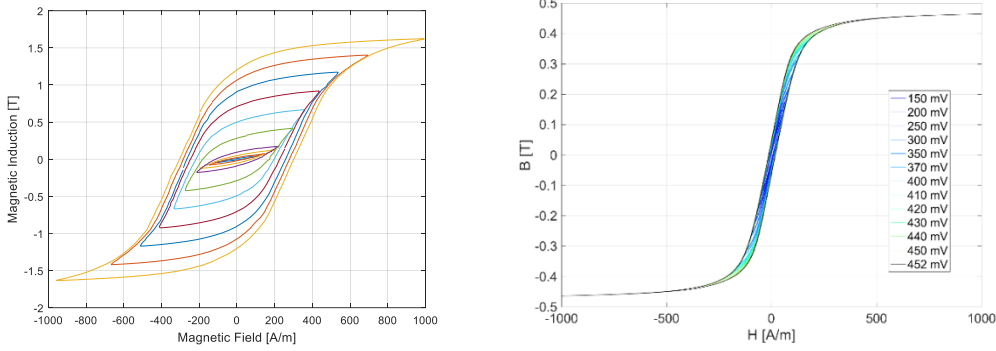


Fig. 5. Left: Hysteresis cycle at 10 Hz of the ferromagnetic samples for different values of the applied voltage (from 100mV up to 2100mV). Right: Hysteresis cycle at 10 Hz of the ferromagnetic yoke.

### 2.2.3. Excitation/detection coil

The HF excitation/detection probe  $N_3$  is a bobbin coil of height 16.7mm, internal radius 1.8mm, external radius 9.4mm. It is formed by 750 copper turns with diameter  $d_c = 0.3 \text{ mm}$ . The resistivity of copper has been measured at room temperature with the 4-probe method and is equal to  $\eta_{Cu} = 1.7 \cdot 10^{-8} \Omega \cdot m$ .

The coil has been fully characterized at different frequencies and different applied currents, both having the same order of magnitude of those applied during the experiments described in Section 4. This is mandatory in view of the comparison with the results from the numerical model. The characterization has been performed by means of a HP4192A Impedance Analyzer giving an equivalent resistance at 5 kHz of  $R_0 = 7.1 \Omega$  and an inductance of  $L_0 = 2.8 \text{ mH}$ . A similar characterization has also been carried out for coil  $N_4$  that has also been used as excitation/detection coil.

### 2.3. Experimental results

The electromagnetic probe has been tested by adopting two different specimens cut from the same ferromagnetic sample and placed between the legs of the yoke (see Fig. 4):

- a) a strip of dimensions  $(250\text{mm} \times 20\text{mm} \times 1.1\text{mm})$ ;
- b) a plate of dimensions  $(400\text{mm} \times 400\text{mm} \times 1.1\text{mm})$ .

In case a) winding  $N_4$  across the strip has been used as both LF (10 Hz) excitation and HF (5 kHz) detection coil, by feeding it with two voltage driven current sources, similar to that depicted in Fig. 4.

In case b) the LF excitation has been applied to winding  $N_1$  via a voltage source (as illustrated in Fig. 4), while coil  $N_3$  has been used as HF excitation and pick-up coil.

The choice is justified by the extremely different field configurations that are likely to appear in the two test samples and that are deemed to be extremely significant for a complete experimental and numerical characterization of the system. In fact, in case a) the LF magnetic field is mainly directed along the straight line connecting the two legs whereas in case b) the LF magnetic field distribution is essentially two-dimensional. In both cases, the LF excitation has a frequency  $f_l = 10 \text{ Hz}$ , which ensures a skin depth  $\delta_s \sim 1.3 \text{ mm}$ . Moreover, it has variable amplitudes in order to establish different working cycles (minor and major, saturated and not saturated loops) in the samples. The HF excitation is a sinusoidal current of amplitude ranging between 3 and 8 mA and frequency  $f_h = 5 \text{ kHz}$ . Preliminarily tests have been performed by turning on only the LF excitation and, only after its effects have been fully clarified, also the HF excitations has been superimposed. In the following sections, the main results of the experimental tests are illustrated and commented.

### 2.3.1. The strip

When performing experiments on the strip, winding  $N_4$  (with 30 turns), has been wound across the strip, and has been used both as LF excitation and HF excitation/pick-up coil (Fig. 4). It allows to gain further information by measuring the induced voltage and deriving the time evolution  $\phi_B(t)$  of the magnetic flux in the test sample. Fig. 6 shows a typical waveform for the LF excitation current  $i_{lf}(t)$ , the input voltage across winding  $N_3$  and the induced voltages across windings  $N_1$  and  $N_2$ . Fig. 7 shows the magnetic flux  $\phi_B(t)$  established both in the yoke and in the ferromagnetic strip. The corresponding hysteresis cycles are plotted too. Results are for an applied sinusoidal LF current  $i_{lf}(t)$  of 1.6 A rms. The applied voltage, as expected, is distorted and the 3<sup>rd</sup> harmonic content, calculated with a Fast Fourier Transform (FFT) algorithm, is about 11% of the fundamental frequency.

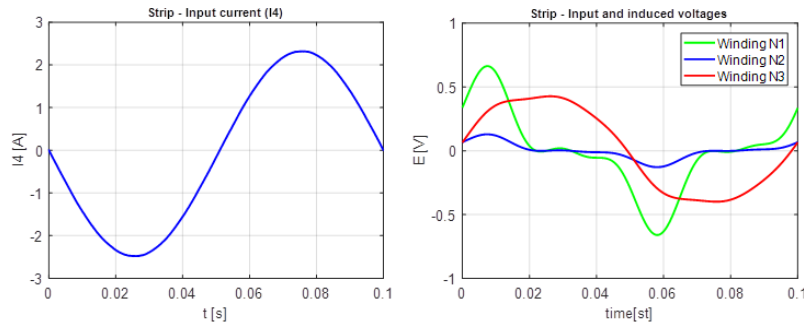


Fig. 6. Left: time evolution of the input current  $I_3$ . Right: time evolution of the input LF voltage (red) and induced voltages  $E_1(t)$  across winding  $N_1$  (green) and  $E_3(t)$  across winding  $N_2$  (blue), due to time varying fluxes

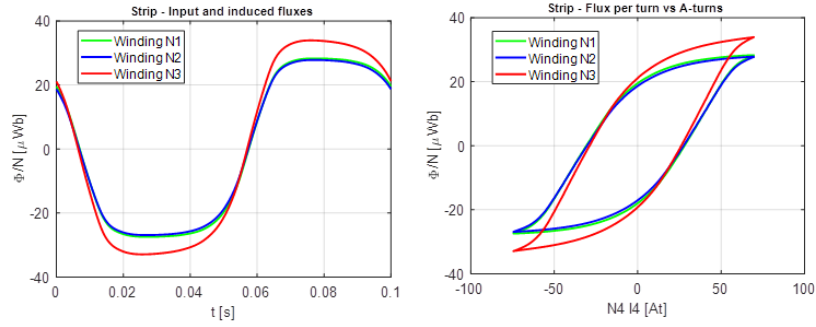


Fig. 7. Left: time evolution of the magnetic flux linked with winding  $N_3$  (red) and induced fluxes linked with winding  $N_1$  (green) and winding  $N_2$  (blue). Right: corresponding hysteresis cycles

In order to detect the variation of the incremental permeability  $\mu_\Delta$  of the sample under test (i.e. the strip), the coil  $N_4$  has been used also as HF excitation/detection coil: it is used to superimpose an incremental field produced by the HF sinusoidal current flowing in the coils. The excitation frequency is  $f_h = 5 \text{ kHz}$ , 500 times higher than the low frequency current driving the hysteresis of the test sample, in order to guarantee at each period a fixed working point on the cycle. The amplitude of the applied current is 9 mA, in order to obtain a magnetic field small enough as to induce reversible magnetization in the sample.

The incremental permeability is not directly measured but, rather, the impedance  $Z$  of winding  $N_4$  is measured, strictly related to  $\mu_\Delta$ . The role of the HF superimposed field is visible in the time evolution of the induced voltage across the pick-up winding  $N_2$  (Fig. 8).

The obtained profile curve of the magnitude  $|Z|$  is shown in Fig. 9. As expected, the curves are almost symmetrical with respect to the  $y$ -axis: the maximum values of the equivalent impedance magnitude are obtained at points (1) and (4) of the working cycle, in which the hysteresis curve has its maximum local steepness. Minimum values (at points 3 and 6) are obtained in correspondance of the maximum value of the excitation ampere-turns.

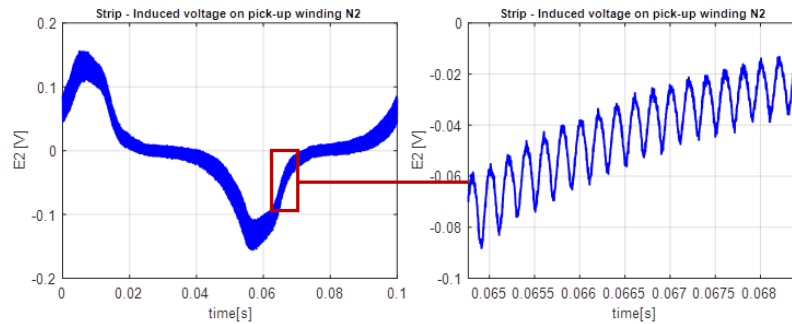


Fig. 8. Time evolution of the induced voltage  $E_2(t)$  across the pick-up winding  $N_2$



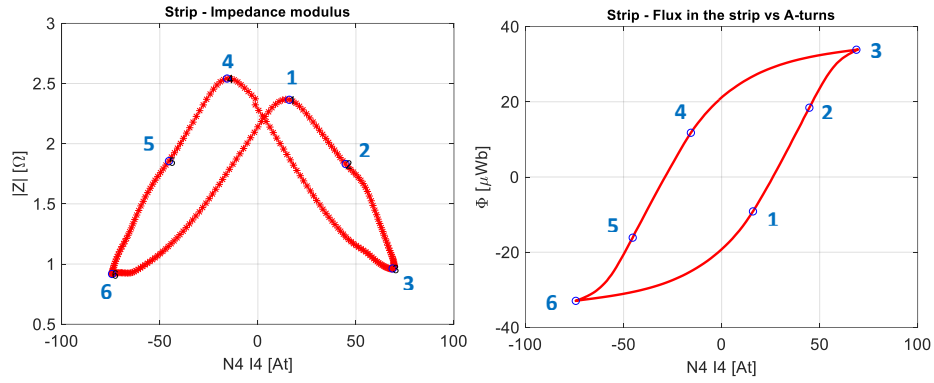


Fig. 9. Right: modulus of the impedance of the HF pick-up coil as a function of the LF excitation current; Left: hysteresis cycle in the strip

### 2.3.2. The plate

A second type of experiment (figs. 10, 11 and 12) has been performed by replacing the ferromagnetic strip with a plate ( $400\text{mm} \times 400\text{mm} \times 1.1\text{mm}$ ) made out of the same material and cut from the same initial slab. In this case, measurements have been carried by applying a LF voltage with rms value  $E_1 = 400\text{ mV}$ . Unfortunately, due to the absence of the pick-up winding  $N_4$ , it is not possible to gain direct information on the magnetic flux across the plate and, consequently, on the test sample LF cycles.

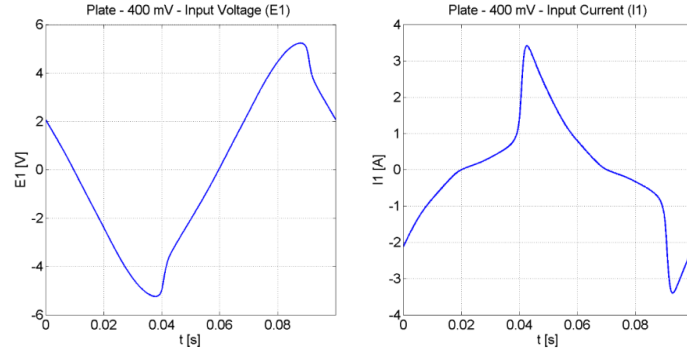


Fig. 10. Time evolution of the LF excitation voltage  $E_1$  and current  $I_1(t)$  for  $E_1 = 400\text{ mV}$

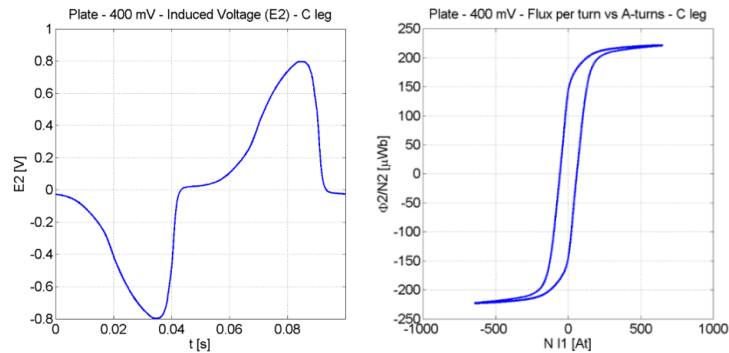


Fig. 11. Left. Time evolution of the LF voltage induced in the C leg, on the pick-up winding  $N_2$ . Right: Flux per turn linked with the pick-up winding  $N_2$  vs the Ampere-turns of the excitation winding for  $E_1 = 400\text{ mV}$

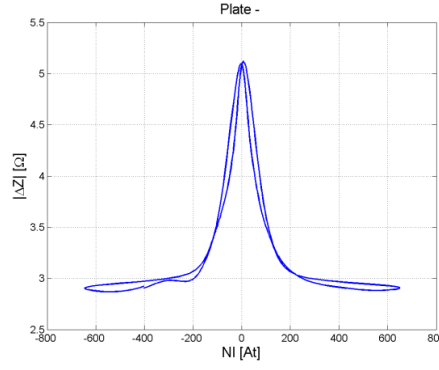


Fig. 12. Modulus of the impedance variation of the HF pick-up coil as a function of the LF Excitation current, for  $E_1 = 400 \text{ mV}$

### 3. Numerical analysis

#### 3.1. Numerical formulation

Here we briefly recall the mathematical model and the related numerical formulation. Further details can be found in [20, 21, 22]. The field problem is described by the following coupled volume integral equations in terms of the field sources, the induced current density vector  $\mathbf{J}$  and the magnetization vector  $\mathbf{M}$ :

$$\int_0^t \eta \mathbf{J}(\mathbf{r}, t) dt + \mathbf{A}_J [\mathbf{J}]|_{(\mathbf{r}, t)} + \mathbf{A}_M [\mathbf{M}]|_{(\mathbf{r}, t)} = -\mathbf{A}_S(\mathbf{r}, t) - \nabla \int_0^t \phi(\mathbf{r}, t) dt, \forall \mathbf{r} \in V_C \text{ and } \forall t \quad (1)$$

$$\mathbf{M}(\mathbf{r}, t) = \mathcal{G} [\mathbf{B}_S(\mathbf{r}, t) + \mathbf{B}_M [\mathbf{M}]|_{(\mathbf{r}, t)} + \mathbf{B}_J [\mathbf{J}]|_{(\mathbf{r}, t)}], \forall \mathbf{r} \in V_M \text{ and } \forall t \quad (2)$$

In Eqs. (1) and (2),  $\mathbf{A}_S$  and  $\mathbf{B}_S$  are the vector potential and the magnetic flux density due to the sources external to the computational domain,  $\mathbf{A}_M$  and  $\mathbf{B}_M$  are the vector potential and the magnetic flux density due to the magnetization whereas  $\mathbf{A}_J$  and  $\mathbf{B}_J$  are the vector potential and the magnetic flux density due to the eddy currents. The discretization of (1) and (2) is obtained with the Galerkin's method. In the conducting domain, we represent  $\mathbf{J}$  as the linear combination of the basis functions  $\mathbf{J}_j = \nabla \times \mathbf{T}_j$  with edge element shape functions for  $\mathbf{T}_j$ , while the magnetization is expanded on piecewise constant functions  $\mathbf{P}_j(\mathbf{r})$  in the magnetic domain [20, 21, 22]. By choosing the  $\mathbf{J}_k$ 's in (2) and the  $\mathbf{P}_k$ 's in (3) as the weighting functions, respectively, we obtain the following nonlinear set of equations in the time domain:

$$\underline{\underline{R}} \underline{I}(t) + \underline{\underline{L}} \frac{d}{dt} \underline{I}(t) = -\underline{\underline{Q}} \frac{d}{dt} \underline{M}(t) - \frac{d}{dt} \underline{U}_S(t) - \underline{\underline{F}} \phi(t) \quad (3)$$

$$\underline{M}(t) = \underline{G} \left[ \underline{B}_S(t) + \underline{\underline{E}} \underline{M}(t) + \underline{\underline{Q}}^T \underline{I}(t) \right] \quad (4)$$

In Eqs (3) and (4),  $\underline{I}(t)$  and  $\underline{M}(t)$  are the column vectors made of the coefficients  $I_j(t)$  and  $M_j(t)$  used in the expansion of the unknowns  $\mathbf{J}$  and  $\mathbf{M}$  in terms of basis functions. The column vector  $\phi$  is made of the voltage

values  $\phi_j$  on each electrode facet  $S_j$ . The relevant matrices/vectors are defined as follows:  $R_{ij} = \int_{V_c} \mathbf{J}_i \cdot \eta \mathbf{J}_j dV$ ,

$$L_{ij} = \int_{V_c} \mathbf{J}_i \cdot \mathbf{A}_j [\mathbf{J}_j] dV, \quad Q_{ij} = \int_{V_c} \mathbf{J}_i \cdot \mathbf{A}_M [\mathbf{M}_j] dV, \quad F_{ij} = \int_{S_j} \mathbf{J}_i \cdot \hat{\mathbf{n}}_j dS, \quad U_{S,i} = \int_{V_0} \mathbf{J}_i \cdot \mathbf{A}_S dV, \quad B_{S,i} = \int_{V_0} \mathbf{J}_i \cdot \mathbf{B}_S dV \quad \text{and}$$

$$E_{ij} = \int_{V_c} \mathbf{M}_i \cdot \mathbf{B}_M [\mathbf{M}_j] dV.$$

The solution of this time-periodic non-linear set of equations with hysteretic media is obtained by applying a fixed-point algorithm in the frequency domain [22, 23]. It can be shown that the resulting iterative procedure is convergent if the magnetic constitutive equation verifies Lipschitz condition and is uniformly monotonic [22, 24, 25]. The advantage, in terms of CPU time guaranteed by this rigorous approach in the frequency domain is enormous, when comparing the number of solutions required in the time domain for reaching steady-state conditions (of the order of the number of time steps) and the number of solutions required in the frequency domain that is of the order of the number of harmonics.

From the numerical point of view, the difficulty of analyzing this case lies in the need to model the response of a complex system produced by two driving currents having frequencies of different orders of magnitude. However, since the field  $\Delta \mathbf{B}$  produced by the high-frequency current is much smaller than the reference field  $\mathbf{B}_0$  at low frequency, the computation can be split in two decoupled problems by performing appropriate linearization [20, 21]. This results in: *i*) a nonlinear (fully hysteretic) magnetic field problem where the driving force is the low-frequency current, which gives the working point  $(\mathbf{M}_0, \mathbf{B}_0)$  at each point  $\mathbf{r}$  in the medium; *ii*) a linear problem for the small change  $(\Delta \mathbf{H}, \Delta \mathbf{B})$  where the inhomogeneous constitutive relation is given by  $\Delta \mathbf{B}(\mathbf{r}) = \mu_{\text{rev}} (\mathbf{M}_0(\mathbf{r}), \mathbf{B}_0(\mathbf{r})) \cdot \Delta \mathbf{H}(\mathbf{r})$ . As a consequence, in the step *ii*), Eqs. (3) and (4) can be rewritten in the frequency domain as:

$$(\underline{R} + j\omega \underline{L}) \underline{\Delta \mathbf{I}} = -j\omega \underline{Q} \underline{\Delta \mathbf{M}} - j\omega \underline{U}_{HF} \quad (5)$$

$$\mu_0 \underline{\Delta \mathbf{M}} = \chi_{\text{rev}} \left[ \underline{B}_{HF} + \underline{E} \underline{\Delta \mathbf{M}} + \underline{Q}^T \underline{\Delta \mathbf{I}} \right] \quad (6)$$

### 3.1.1. Vector hysteresis model

The nonlinear constitutive relation  $\mathbf{M} = \mathcal{G}[\mathbf{B}]$  is here given by the isotropic vector generalization of the classical Jiles-Atherton model [26], applied in the analysis of NDE configurations [19, 20, 21, 22].

The input-output relationship between the magnetic induction  $\mathbf{B}$  and the magnetization  $\mathbf{M}$  of the inverse vector Jiles-Atherton hysteresis model is described by the following differential relationships [27], [28], [29]:

$$d\mathbf{M} = \underline{\underline{\chi}}_{\text{irr}} \cdot \frac{d\mathbf{B}}{\mu_0}, \quad \text{if } \underline{\underline{\chi}}_f \cdot d\mathbf{H}_e \geq 0 \quad (7)$$

$$d\mathbf{M} = \underline{\underline{\chi}}_{\text{rev}} \cdot \frac{d\mathbf{B}}{\mu_0}, \quad \text{if } \underline{\underline{\chi}}_f \cdot d\mathbf{H}_e < 0 \quad (8)$$

where

$$\underline{\underline{\chi}}_{\text{irr}}(\mathbf{M}_0, \mathbf{B}_0) = \left[ \underline{\underline{I}} + (1-\alpha)\underline{\underline{D}} + c(1-\alpha)\underline{\underline{\xi}} \right]^{-1} \left[ \underline{\underline{D}} + c\underline{\underline{\xi}} \right] \quad (9)$$

$$\underline{\underline{\chi}}_{\text{rev}}(\mathbf{M}_0, \mathbf{B}_0) = \left[ \underline{\underline{I}} + c(1-\alpha)\underline{\underline{\xi}} \right]^{-1} \left[ c\underline{\underline{\xi}} \right] \quad (10)$$

are the differential susceptibility matrices associated with small magnetization changes  $d\mathbf{M}$  produced by small magnetic induction changes  $d\mathbf{B}$  at the point  $(\mathbf{M}_0, \mathbf{B}_0)$ ,

$$\underline{\underline{\chi}}_f = \frac{\mathbf{M}_{\text{an}} - \mathbf{M}}{k}, \quad d\mathbf{H}_e = \frac{d\mathbf{B}}{\mu_0} + (\alpha-1)d\mathbf{M}, \quad \underline{\underline{D}} = \underline{\underline{\chi}}_f \underline{\underline{\chi}}_f^T | \underline{\underline{\chi}}_f |^{-1}, \quad (11)$$

$$\underline{\underline{\xi}} = \text{diag} \left[ \frac{\partial \mathbf{M}_{\text{an}}}{\partial \mathbf{H}_e} \right], \quad \mathbf{M}_{\text{an}}(\mathbf{H}_e) = M_s \left[ \coth \frac{|\mathbf{H}_e|}{a} - \frac{a}{|\mathbf{H}_e|} \right] \frac{\mathbf{H}_e}{|\mathbf{H}_e|}, \quad (12)$$

$\underline{\underline{I}}$  is the identity matrix,  $M_s, k, c, \alpha, a$ , are the parameters of the classical (scalar) Jiles-Atherton model and  $\mathbf{M}_{\text{an}}(\mathbf{H}_e)$  is the vector generalization of the anhysteretic magnetization curve.

By using Eqs. (9) and (10), it is possible to compute the differential permeability tensor in any point of the material as follows (the dependence on  $(\mathbf{M}_0, \mathbf{B}_0)$  is understood):

$$\underline{\underline{\mu}}_{\text{irr}} = \mu_0 (\underline{\underline{I}} - \underline{\underline{\chi}}_{\text{irr}})^{-1}, \quad \text{if } \underline{\underline{\chi}}_f \cdot d\mathbf{H}_e \geq 0 \quad (13)$$

$$\underline{\underline{\mu}}_{\text{rev}} = \mu_0 (\underline{\underline{I}} - \underline{\underline{\chi}}_{\text{rev}})^{-1}, \quad \text{if } \underline{\underline{\chi}}_f \cdot d\mathbf{H}_e < 0. \quad (14)$$

Typically, the  $3 \times 3$  matrix expressed by Eq. (13) is fully populated whereas the reversible permeability matrix (14) is diagonal but not isotropic.

The latter equation plays an essential role for the simulation of the incremental permeability measurement technique.

### 3.1.2. Incremental permeability

In order to use the vector JA hysteresis model for the analysis of differential permeabilities in complex finite-element studies, some considerations on how the model fulfills general vector hysteresis properties are needed.

In fact, first of all one would expect that an isotropic and initially demagnetized material, subject to a magnetic induction field  $\mathbf{B}$  with sinusoidal amplitude and directed along a given orientation  $\mathbf{b}$ , should produce in steady-state conditions a periodic magnetic field  $\mathbf{H}$  aligned with the same direction. Moreover, the components of  $\mathbf{B}$  and  $\mathbf{H}$  projected along the direction  $\mathbf{b}$ , when represented on a Cartesian diagram, should give rise, in principle, to the same hysteresis loop regardless of the particular choice of  $\mathbf{b}$ . This property is often referred to as reduction of vector hysteresis to scalar hysteresis [30].

An additional qualitative feature concerning differential permeabilities is also expected as a consequence of the isotropy of the material. In fact, as outlined above, let us assume to be in steady-state conditions describing a hysteresis loop along the chosen direction  $\mathbf{b}$  and stopping at a given field amplitude  $B_0$ . Then, let us consider the differential permeabilities along generic directions  $\mathbf{b}_\perp$  lying in the plane perpendicular to  $\mathbf{b}$ . Again, one would expect that such permeabilities do not depend on the particular choices of both  $\mathbf{b}$  and  $\mathbf{b}_\perp$ . This property is connected to the correlation of mutually orthogonal components of input and output fields in vector hysteresis [30].

These considerations appear quite natural and reasonable based on the hypothesis of isotropic material, but become considerably challenging when vector hysteresis models are introduced. For instance, it is worth mentioning that vector hysteresis models based on the superposition of angularly-distributed classical scalar Preisach models require to fulfill nontrivial mathematical constraints (integral equations) in order to comply with the property of reduction to scalar hysteresis [30]. Thus, in order to circumvent such complex mathematical and computational issues, special classes of hysteresis models naturally fulfilling the latter property and additional qualitative features of vector hysteresis have been introduced (for instance see refs. [31], [32], [33] and references therein).

The vector JA model is computationally efficient due to its local memory property, but, in spite of its simplicity, it exhibits limitations when the reproduction of vector hysteresis features is concerned. In order to make quantitative estimate of these limitations, we have performed two simple tests of the vector JA model (the parameters are  $M_s = 1.54 \times 10^6 \text{ A/m}$ ,  $a = 445$ ,  $k = 290$ ,  $\alpha = 0.00077$ ,  $c = 0.02$ ) for the calculation of differential permeabilities, as outlined above by changing the orientations  $\mathbf{b}$  and  $\mathbf{b}_\perp$ . Each test consists of 3 stages: 1) apply sinusoidal magnetic induction (amplitude 1 T) along a given direction  $\mathbf{b}$  and describe 3 full scalar hysteresis loops until a final value  $B_0$ ; 2) apply a sinusoidal magnetic induction with small amplitude 1 mT along a direction transverse to  $\mathbf{b}$ , namely  $\mathbf{b}_\perp = \mathbf{a} \times \mathbf{b}$ ; 3) evaluate differential permeability along the direction  $\mathbf{b}_\perp$ . We will refer to tests T1 and T2 where choices of  $\mathbf{b}$  and  $\mathbf{b}_\perp$  are reported in fig. 13.

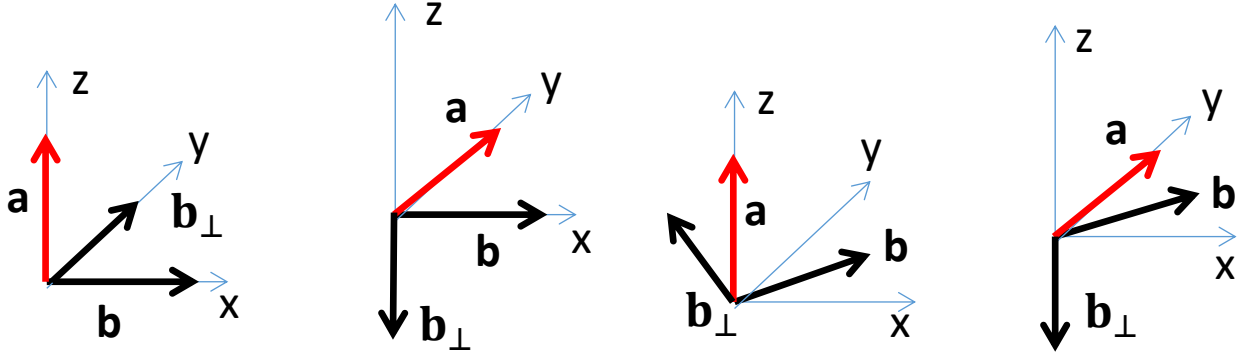


Fig. 13. Sketch of directions  $\mathbf{b}$ ,  $\mathbf{b}_\perp$  used in tests T1 (left-two) and T2 (right-two) to compare differential permeabilities.

The calculation is repeated twice for each test by selecting  $B_0$  close to saturation (T1.1, T2.1) and corresponding to coercive field (T1.2, T2.2), respectively. The results of the computations are reported in Table I.

Table I: Results of differential permeabilities computation with the vector JA model

	T1.1	T1.2	T2.1	T2.2
$\mathbf{b}$	(1,0,0)	(1,0,0)	$(\sqrt{2}/2, \sqrt{2}/2, 0)$	$(\sqrt{2}/2, \sqrt{2}/2, 0)$
$\mathbf{b}_\perp$	(0,1,0) (0,0,-1)	(0,1,0) (0,0,-1)	$(-\sqrt{2}/2, \sqrt{2}/2, 0)$ (0, 0, -1)	$(-\sqrt{2}/2, \sqrt{2}/2, 0)$ (0, 0, -1)
$B_0$	1T	0T	1T	0T
$H_0$	559.07 A/m	-270.91 A/m	557.57 A/m	-270.79 A/m
$\mu_\perp$	2.2581e-005 2.2581e-005	3.005e-005 3.005e-005	1.7853e-005 2.2592e-005	2.9443e-005 3.0051e-005

From the analysis of the results, some conclusions can be drawn. First, we observe that the values of field  $H_0$  agree between T1 and T2 with a small relative error below 1%. Thus, the reduction to scalar hysteresis is fairly well reproduced by the vector JA model. Then, as far as the invariance of the differential permeabilities is concerned, we notice that agreement is very good between T1 and T2 when the scalar hysteresis occurs along a coordinate axis (relative error much below  $10^{-3}$ ). Conversely, the maximum stressful condition for the model is realized when the scalar hysteresis occurs along an orientation tilted  $45^\circ$  off the  $x$ -axis, which yield a relative error up to 20% in the computed permeabilities with field close to saturation (T2.1). Further tests (not reported) performed with  $\mathbf{a}$  and  $\mathbf{b}$  tilted  $45^\circ$  off in the  $yz$  and  $xy$  plane, respectively, exhibit the same results as T2.1 and T2.2 (largest error with field at saturation).

### 3.2. Numerical analysis of the strip

The geometry of the ferromagnetic joke is illustrated in Fig. 4. The finite element discretization ( $a \times b \times \Delta = 233\text{mm} \times 22.4\text{mm} \times 1.1\text{mm}$ , 7124 elements,  $N_f=30$  electrical unknowns,  $N_M=15072$  magnetic unknowns for each Fourier harmonic,  $N_f=11$  Fourier harmonics leading to  $N_{DOF}=(N_f+ N_M) \times N_f = 169092$  complex unknowns for the LF excitation) is shown in Fig. 14. The parameters of the Jiles-Atherton model are  $c=0.23$ ,  $a=750$ ,  $k=1600$ ,  $M_s=1.3 \times 10^6$  A/m,  $\alpha=1.8 \times 10^{-3}$ . In Fig. 15, the low frequency current and voltage

measured at the input of the winding N3 are compared with the experiment. Notice that the voltage is assumed in input and decomposed in a number of harmonics (11 in this specific case), while the current represent the numerically computed solution. In Fig. 16, the measurements reproducing a cycle of hysteresis in the ferromagnetic yoke is shown and compared with the same data numerically computed. They are measured and computed by using the coil N2.

To compute the response of the system to the HF excitation, we impose the reversible permeability tensor (14) in each point of the ferromagnetic plate, for a set of 50 working points along the hysteresis curve.

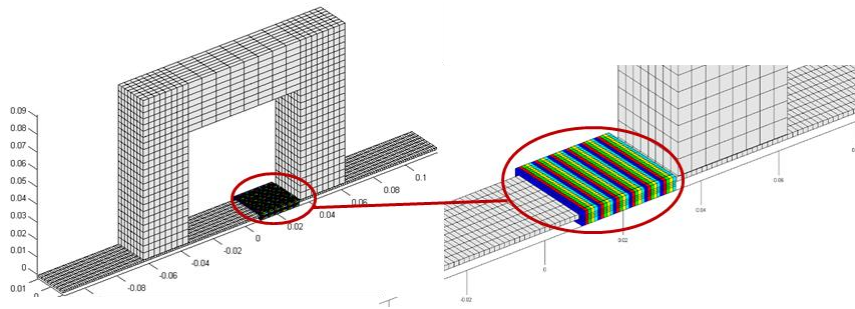


Fig. 14. The finite element mesh used for the LF computation. On the right, a zoom of the winding N3

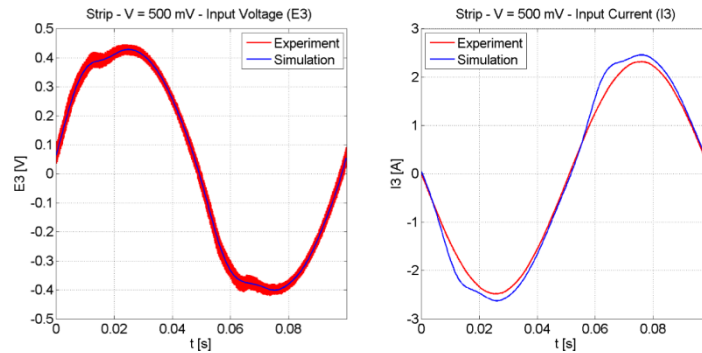


Fig. 15. Time evolution of the input voltage  $V_3$  (left, red), and of the input current (right): Simulation vs experimental data

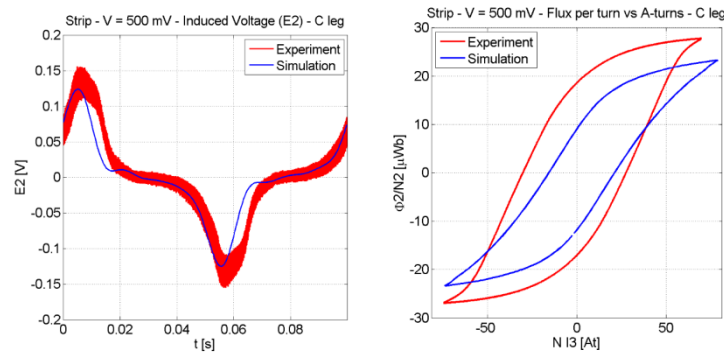


Fig. 16. Left: time evolution of the induced voltage  $E_2$  on the C-leg Right: flux linked with the pick-up winding  $N_2$  as a function of the LF input Ampere-turns

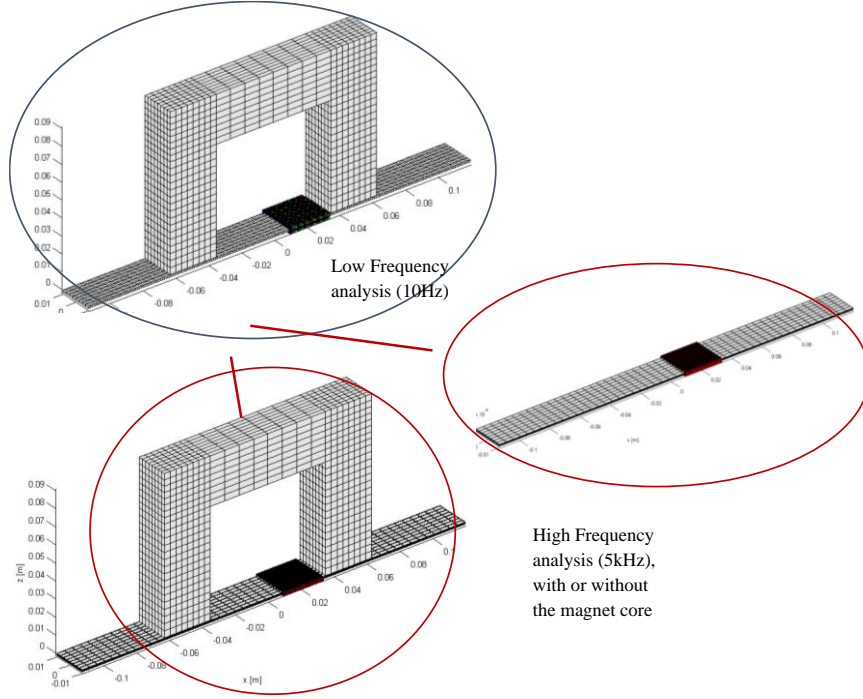


Fig. 17. The finite element mesh used for the HF computation, with and without the ferromagnetic yoke.

For each working point ( $\mathbf{M}_0(\mathbf{r}), \mathbf{B}_0(\mathbf{r})$ ), the linear magneto-quasistatic system given by (5) and (6) is solved. In this case, the discretization of the strip is different (see Figure 17) because it should take into account the constraint imposed by the skin effect related to the HF excitation ( $a \times b \times \Delta = 233\text{mm} \times 20\text{mm} \times 1.1\text{mm}$ , 17984 elements,  $N_j=12957$  electrical unknowns,  $N_M=32352$  magnetic unknowns). In order to estimate the effect of the yoke on the computation, we carried out the analysis with and without the magnetic core.

The differential permeability at each working point of the magnetic curve is shown in Fig. 18. The HF impedance variation, computed with and without the ferromagnetic core and compared with the measurements is shown in Fig. 19. Because the HF windings is the same as the low frequency winding, it can be seen that the presence of the magnetic core gives a significant, contribution in this case. Moreover the agreement on the imaginary part of the impedance variation is fairly good, while a large discrepancy is present between the numerical value of its real part and the experiment.

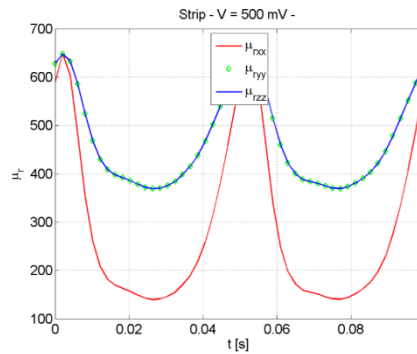


Fig. 18. The differential permeability at each working point of the magnetic curve, as a function of time.



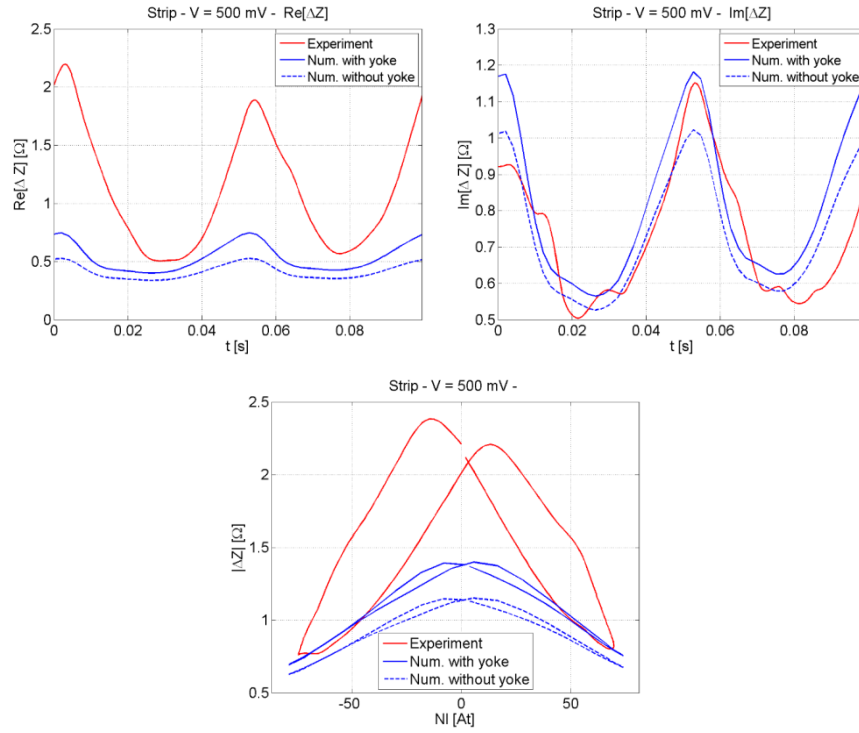


Fig. 19. Time evolution of the HF impedance of the pickup coil wound around the strip (left top: real part, right top: imaginary part; bottom: modulus). The measurements are compared with the computed results with and without the ferromagnetic yoke

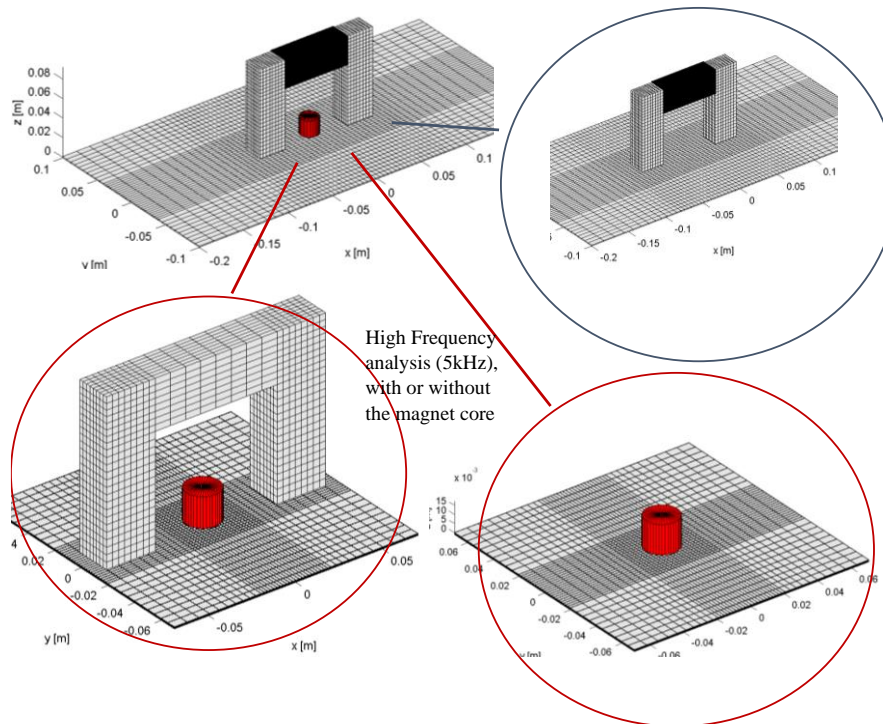


Fig. 20. The finite element mesh used for the LF and HF computation.

### 3.3. Numerical analysis of the plate

As in the previous case, we performed the analysis in two steps. First, we compute the working points according to the Low Frequency excitation. In this step, the plate is characterized only by its magnetic properties and therefore the eddy currents are neglected. The mesh ( $a \times b \times \Delta = 400\text{mm} \times 200\text{mm} \times 1.1\text{mm}$ , 13549 elements,  $N_j = 190$  electrical unknowns in the winding,  $N_M = 18717$  magnetic unknowns for each Fourier harmonic,  $N_f = 11$  Fourier harmonics leading to  $N_{DOF} = (N_j + N_M) \times N_f = 207977$  complex unknowns for the LF excitation) is shown in Fig. 20. The input voltage is imposed and the input current is computed and compared with the measurements in Fig. 21, while in Fig. 22 the voltage induced in the winding N2 is shown and again compared with the experiment. In Fig. 23, the anisotropic differential permeability computed by using the vector Jiles Atherton model presented in the previous section is shown, as computed in a specific element between the legs of the ferromagnetic core.

These values of the magnetic permeability are then imposed in the plate that is discretized in finer way, since now the eddy currents play a dominant role. The dimensions of the plate have been reduced with respect to the LF case ( $a \times b \times \Delta = 140\text{mm} \times 140\text{mm} \times 1.1\text{mm}$ ), but its discretization, shown in Fig. 20, is finer (19460 elements, 15876 without the yoke,  $N_j = 29233$  electrical unknowns,  $N_M = 58380$  magnetic unknowns, 47628 without the yoke). In this limit, we have to solve a linear problem in the frequency domain for each magnetic working point. The results for the impedance variation are shown in Fig. 24. In this figure, it can be seen that the results obtained by imposing the isotropic permeability  $\mu_{diff} = \mu_{xx}$ , where the x-axis is in the dominant direction of the LF magnetic field, are much better than those obtained by using the anisotropic diagonal tensor  $diag[\mu_{xx}, \mu_{yy}, \mu_{zz}]$ . A possible explanation has been outlined in the previous section. Finally, we remark that in this case the presence of the yoke does not affect the results.

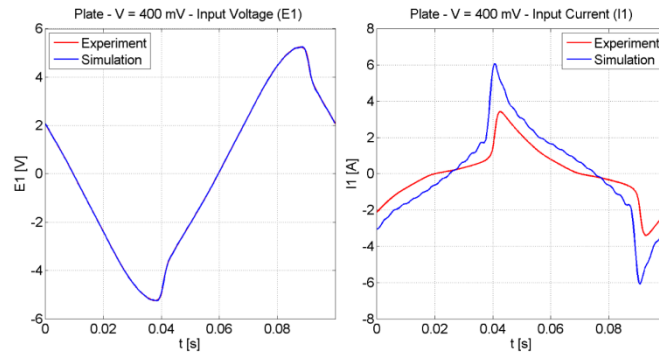


Fig. 21. Time evolution of the input voltage  $V_1$  (left, red), and of the input current (right): Simulation vs experimental data.

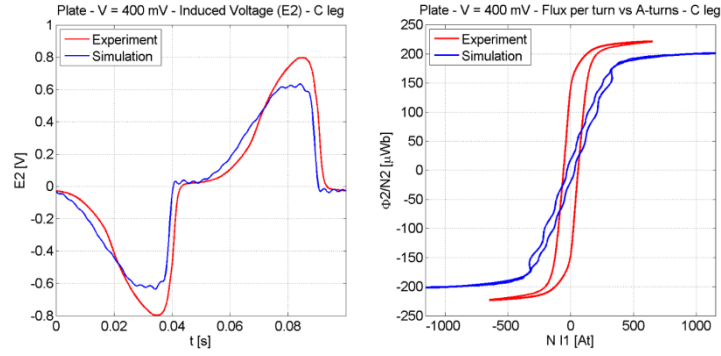


Fig. 22. Left: time evolution of the induced voltage  $E_2$  on the C-leg. Right: flux linked with the pick-up winding  $N_2$  as a function of the LF input Ampere-turns.

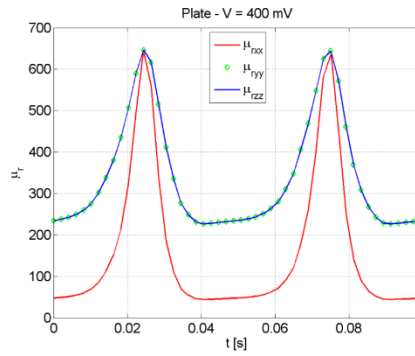


Fig. 23. The anisotropic differential permeability at each working point of the magnetic curve, as a function of time.

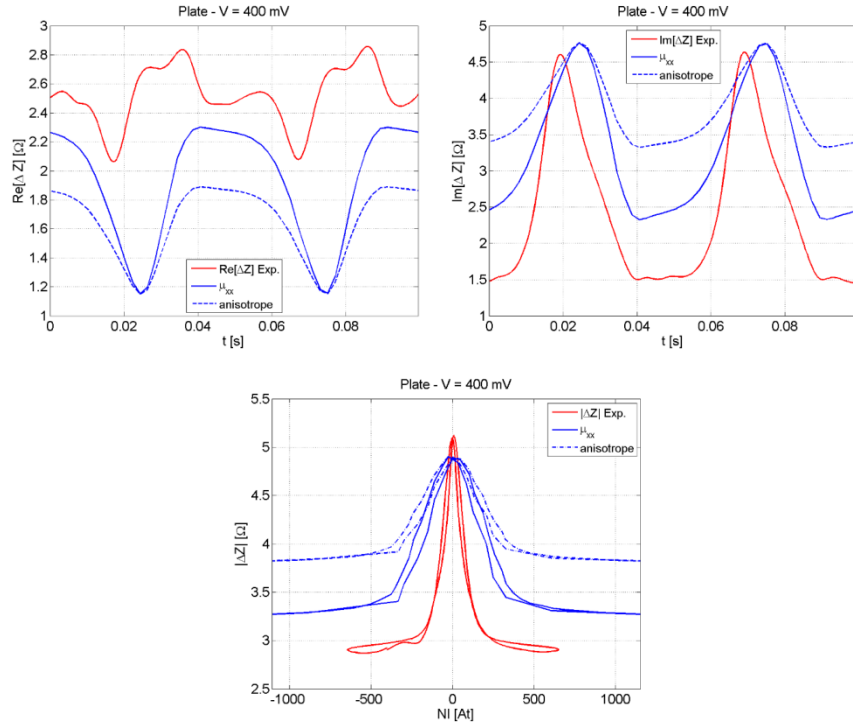


Fig. 24. Time evolution of the HF impedance of the pickup coil (left top: real part, right top: imaginary part; bottom: modulus). The measurements are compared with the computed results without the ferromagnetic yoke.

#### **4. Conclusions**

In this work we presented an extensive and detailed experimental campaign to validate a full 3D numerical model, specifically developed for Micromagnetic Measurements of ferromagnetic materials. Micromagnetic Measurements play an important role in Material Characterization of ferromagnetic materials thanks to their correlation to mechanical properties. This gives to Micromagnetic Measurements a key role in steel industry.

The numerical model described in this work is capable to treat ferromagnetic materials with magnetic hysteresis. The model is capable of treating a complex phenomenon such as the vector hysteresis. Moreover, the numerical model is capable to account for the electrical conductivity of the material. This makes the problem even more complex because of the presence of the skin-effect. The numerical model has been specifically developed and optimized for arbitrary periodic regimes.

The experimental validation has been carried out with reference to two important types of analysis on ferromagnetic materials. The first one is the harmonic analysis, where a “low” frequency (10Hz) strong field is applied to the ferromagnetic material. This strong field brings the ferromagnetic to saturation. The second analysis is related to the incremental permeability, where one measures the impedance of a “high” (5kHz) frequency coil at different points of the hysteresis loop. This is achieved by measuring the impedance of this pick-up coil (at 5kHz) when driving the system along a hysteresis loop with the “strong” low frequency (10Hz) field. Due to the vectorial nature of the hysteresis, the differential permeability is better described by a tensor. The numerical model contributes in disclosing the connection between the actual permeability and the measured quantity (the impedance of the coil).

#### **Acknowledgement**

The authors recognize the valuable contribution of Dr. Massimo Attanasio for the set-up realization and management at the Circuits Laboratory of Electrical Engineering Department, University of Naples FEDERICO II. **Ciro Visone e Daniele Davino**

#### **5. References**

- [1] D. C. Jiles, Magnetic methods in nondestructive testing, K. H. J. Bushow (Ed.), Encyclopedia of materials science and technology, Elsevier Press, Oxford (2001).
- [2] Dobmann, G., Altpeter, I., Wolter, B., Kern, R., “Industrial applications of 3MA - Micromagnetic multiparameter microstructure and stress analysis”, Studies in Applied Electromagnetics and Mechanics, 31, pp. 18-25, 2008.
- [3] O. Perevertov, M. Neslušán, A. Stupakov, “Detection of milled 100Cr6 steel surface by eddy current and incremental permeance methods”, NDT & E International, Volume 87, Pages 15-23, 2017.
- [4] Szielasko, K., Mironenko, I., Altpeter, I., Herrmann, H.-G., Boller, C., “Minimalistic devices and sensors for micromagnetic materials characterization”, IEEE Transactions on Magnetics, 49 (1), art. no. 6392425, pp. 101-104, 2013.

- [5] Szielasko, K., Youssef, S., Niese, F., Weikert, M., Sourkov, A., Altpeter, I., Herrmann, H.-G., Dobmann, G., Boller, C., "Multi-method probe design for the electromagnetic characterization of advanced high strength steel", *Studies in Applied Electromagnetics and Mechanics*, 39, pp. 52-59, 2014.
- [6] Dobmann, G., Boller, C., Herrmann, H.-G., Altpeter, I., "Micromagnetic and electromagnetic NDT for lifetime management by monitoring ageing of structural materials", (2014) *International Journal of Microstructure and Materials Properties*, 9 (3-5), pp. 348-359.
- [7] Altpeter, I., Dobmann, G., Hübschen, G., Kopp, M., Tschuncky, R., "Nondestructive characterization of neutron induced embrittlement in nuclear pressure vessel steel microstructure by using electromagnetic testing", *Studies in Applied Electromagnetics and Mechanics*, 35, pp. 322-329, 2011.
- [8] S. Takahashi, S. Kobayashi, I. Tomáš, L. Dupre, G. Vértesy, Comparison of magnetic nondestructive methods applied for inspection of steel degradation, *NDT & E International*, Volume 91, Pages 54-60, 2017.
- [9] Gábor Vértesy, Tetsuya Uchimoto, Toshiyuki Takagi, Ivan Tomáš, Hidehiko Kage, "Nondestructive characterization of flake graphite cast iron by magnetic adaptive testing", *NDT & E International*, Volume 74, Pages 8-14, 2015.
- [10] G. Vértesy, I. Mészáros, I. Tomáš, "Nondestructive magnetic characterization of TRIP steels", *NDT & E International*, Volume 54, Pages 107-114, 2013.
- [11] Matsumoto, T., Uchimoto, T., Takagi, T., Szielasko, K., Rabung, M., "Nondestructive Evaluation of Structural Change due to Creep Degradation in P91 Steel by Micromagnetic Properties", (2017) *Studies in Applied Electromagnetics and Mechanics*, 42, pp. 52-60.
- [12] Skarlatos, A., Theodoulidis, T. "Study of the non-linear eddy-current response in a ferromagnetic plate: Theoretical analysis for the 2D case", *NDT and E International*, Volume 93, pp. 150-156, 2018.
- [13] Gupta, B., Ducharne, B., Sebald, G., Uchimoto, T. "A Space Discretized Ferromagnetic Model for Non-Destructive Eddy Current Evaluation", (2018) *IEEE Transactions on Magnetics*, 54 (3), art. no. 6200204.
- [14] Chen, H.-E., Xie, S., Zhou, H., Chen, Z., Uchimoto, T., Takagi, T., Kensuke, Y., "Numerical simulation of magnetic incremental permeability for ferromagnetic material", *International Journal of Applied Electromagnetics and Mechanics*, 45 (1-4), pp. 379-386, 2014.
- [15] Zhang, B., Gupta, B., Ducharne, B., Sebald, G., Uchimoto, T., "Dynamic Magnetic Scalar Hysteresis Lump Model Based on Jiles-Atherton Quasi-Static Hysteresis Model Extended With Dynamic Fractional Derivative Contribution", *IEEE Transactions on Magnetics*, Article in Press, (2018).
- [16] Zhang, B., Gupta, B., Ducharne, B., Sebald, G., Uchimoto, T., "Preisach's model extended with dynamic fractional derivation contribution", *IEEE Transactions on Magnetics*, 54 (3), art. no. 8081796, 2018.
- [17] Adly, A.A., Abd-El-Hafiz, S.K., "An efficient hysteresis modeling methodology and its implementation in field computation applications", *Journal of Magnetism and Magnetic Materials*, 434, pp. 151-156, 2017.
- [18] Malczyk, R., Izydorczyk, J., "The frequency-dependent Jiles-Atherton hysteresis model", *Physica B: Condensed Matter*, 463, pp. 68-75, 2015.
- [19] A. Yashan, G. Dobmann, "Measurements and semi-analytical modeling of incremental permeability using eddy current coil in the presence of magnetic hysteresis", *Studies in Applied Electromagnetics and Mechanics*, Vol. 23, *Electromagnetic Nondestructive Evaluation (VI)*, IOS Press, pp. 150-157, 2002

- [20] M. d'Aquino, S. Minucci, C. Petrarca, G. Rubinacci, A. Tamburrino, S. Ventre, "3D efficient simulation of a magnetic probe for characterization of ferromagnetic specimens", *Studies in Applied Electromagnetics and Mechanics*, Vol. 40, Electromagnetic Nondestructive Evaluation (XVIII), IOS Press, pp. 11-19, 2015.
- [21] M. d'Aquino, G. Rubinacci, A. Tamburrino, S. Ventre, "Three-dimensional computation of magnetic fields in hysteretic media with time-periodic sources", *IEEE Transactions on Magnetics*, 2014, 50, 7001104.
- [22] M. d'Aquino, G. Rubinacci, A. Tamburrino, S. Ventre, Efficient numerical solution of magnetic field problems in presence of hysteretic media for nondestructive evaluation, *IEEE Transactions on Magnetics*, 2013, 49, 3167-3170
- [23] I. R. Ciric, F. I. Hantila, "An efficient harmonic method for solving nonlinear time-periodic eddy-current problems", *IEEE Trans. Magn.*, vol. 43, pp. 1185-1188, Apr. 2007.
- [24] R. Albanese, F. I. Hantila, and G. Rubinacci, "A nonlinear eddy current integral formulation in terms of a two-component current density vector potential", *IEEE Trans. Magn.*, vol. 32, p. 784-787, 1996.
- [25] R. Albanese and G. Rubinacci, "Finite Element Methods for the Solution of 3D Eddy Current Problems", *Advances in Imaging and Electron Physics*, vol. 102, pp. 1-86, 1998.
- [26] D. C. Jiles and D.L. Atherton, "Theory of ferromagnetic hysteresis", *J. Appl. Phys.* vol.55, pp. 2115, 1984.
- [27] A. J. Bergqvist, "A simple vector generalization of the Jiles-Atherton model of hysteresis", *IEEE Trans. Magn.*, vol.32, p. 4213-4215, 1996.
- [28] J. V. Leite, N. Sadowski, P. Kuo-Peng, N. J. Batistela, J. P. A., Bastos and A. A. de Espíndola, "Inverse Jiles-Atherton vector hysteresis model", *IEEE Trans. Magn.*, vol. 40, no. 4, pp. 1769-1775, 2004.
- [29] M. d'Aquino, S. Minucci, C. Petrarca, G. Rubinacci, A. Tamburrino, S. Ventre, "On the experimental validation of a numerical model of a magnetic probe for material characterization", *Advances in Magnetism Conference (AIM 2016)*, Bormio, 2016
- [30] I. D. Mayergoyz, *Mathematical Models of Hysteresis*. New York: Springer, 1991.
- [31] A. Bergqvist, "Magnetic vector hysteresis model with dry friction-like pinning," *Phys. B.* vol. 233, no. 4, pp. 342-347, 1997.
- [32] C. Serpico, M. d'Aquino, C. Visone, D. Davino, "A new class of Preisach-type isotropic vector model of hysteresis," *Physica B*, vol. 343, pp. 117-120, 2004.
- [33] C. Serpico, M. d'Aquino, C. Visone and A. Adly, "A New Vector Model of Magnetic Hysteresis Based on a Novel Class of Play Hysterons," *IEEE Trans. Magn.*, Vol. 39, No.5, pp. 2537-2539, 2003.